ACS NANO
www.acsnano.org
ARTICLE

Mesoporous $Li_xMn_2O_4$ Thin Film Cathodes for Lithium-Ion Pseudocapacitors

Benjamin K. Lesel,[†] Jesse S. Ko,[‡] Bruce Dunn,*[,‡,§] and Sarah H. Tolbert*[,†,‡,§]

[†]Department of Chemistry and Biochemistry, [‡]Department of Materials Science and Engineering, and [§]The California NanoSystems Institute, UCLA, Los Angeles, California 90095, United States

Supporting Information

ABSTRACT: Charge storage devices with high energy density and enhanced rate capabilities are highly sought after in today's mobile world. Although several high-rate pseudocapacitive anode materials have been reported, cathode materials operating in a high potential range *versus* lithium metal are much less common. Here, we present a nanostructured version of the well-known cathode material, $LiMn_2O_4$. The reduction in lithium-ion diffusion lengths and improvement in rate capabilities is realized through a combination of nanocrystallinity and the formation of a 3-D porous framework. Materials were fabricated from nanoporous Mn_3O_4 films made by block copolymer templating of preformed nanocrystals. The nanoporous Mn_3O_4 was then converted *via* solid-state reaction with LiOH to nanoporous $Li_xMn_2O_4$ ($1 < x < 2$). The resulting films had a wall thickness of ~15 nm, which is small enough to be impacted by inactive surface sites. As a consequence, capacity was reduced by about half compared to bulk $LiMn_2O_4$, but both charge and discharge kinetics as well as cycling stability were improved significantly. Kinetic analysis of the redox reactions was used to verify the pseudocapacitive mechanisms of charge storage and establish the feasibility of using nanoporous $Li_xMn_2O_4$ as a cathode in lithium-ion devices based on pseudocapacitive charge storage.

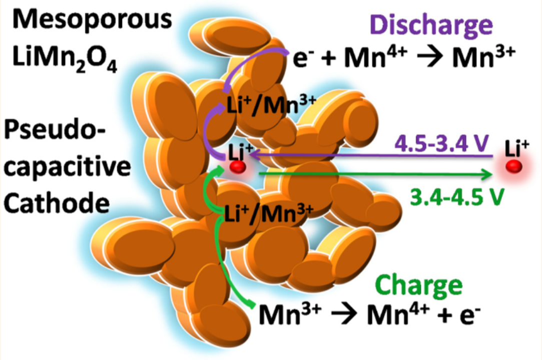

KEYWORDS: *$LiMn_2O_4$, pseudocapacitor, lithium-ion battery, high rate, mesoporous, cathode, nanocrystal templated*

Pseudocapacitive charge storage has the potential to allow for faster charge−discharge rates than conventional battery materials while retaining energy densities much greater than that found in double-layer-type supercapacitors.[1] In a lithium-ion battery material, the kinetics of charge storage are controlled by diffusion of lithium ions within the structure. Intercalation occurs when lithium ions insert into the structure and diffuse to an accessible redox site; for micron-sized powders, long diffusion lengths correlate with slow intercalation kinetics. Pseudocapacitance describes similar redox reactions but without the slow diffusion kinetics. For many years, the term pseudocapacitance was synonymous with surface redox reactions, but more recently, the concept of intercalation pseudocapacitance has been proposed. Extraction/intercalation pseudocapacitance occurs primarily in nanostructured materials when lithium-ion diffusion rates are fast and when diffusion distances are short.[2,3] The primary advantage of intercalation pseudocapacitance is that it utilizes the bulk of the nanostructured material, not just the surface, thus allowing greater energy density to be realized in combination with increased power density.[3−5] To date, intercalation pseudocapacitance has been seen in a number of nanostructured anodes, including α-MoO_3 and T-Nb_2O_5.[2−4] Most of these are layered materials that can accommodate lithium-ion diffusion between the layers.[2,3,6−13] Nb_2O_5, in particular, has an open lattice that allows for fast lithium-ion diffusion without significant structural change.[14] The lack of structural change is good not only because it circumvents diffusion limitations associated with the development of new phases but also because it apparently prevents degradation of the material, allowing for long cycling lifetimes.[3,7,12] To date, however, most quantified examples of intercalation pseudocapacitance have been with materials that show redox in potential ranges more suitable for applications as anode materials rather than as cathode materials. To make a functioning pseudocapacitive device that shows both high energy and power density, we need to extend these phenomena to materials that show redox in higher potential ranges, and that goal is the motivation for the work presented here.

Currently, $LiCoO_2$ is the most widely used cathode material for lithium-ion batteries. Although $LiCoO_2$ along with other materials of the form $LiMO_2$ (where M is a transition metal) are layered and show good cycling stability in bulk, they do not show reliable cycling stability when nanostructured for fast lithium-ion intercalation.[15−17] One reason for this is that the

Received: April 18, 2016
Accepted: July 29, 2016
Published: July 29, 2016

DOI: 10.1021/acsnano.6b02608
ACS Nano 2016, 10, 7572−7581

insertion and removal of lithium ions results in a phase transition between trigonal and monoclinic lattice structures.[15−17] Aside from the lack of rapid diffusion kinetics, $LiMO_2$ materials are known to operate in the 3−4 V range *versus* lithium metal.[17,18] To increase this potential range above 4 V, while maintaining structural stability, one option appears to be the mixed-valent transition metal spinel $LiMn_2O_4$.[19−34] $LiMn_2O_4$ shows activity in the 4−4.5 V range with reasonable structural robustness upon cycling. The structure contains lithium ions within tetrahedral sites that can be repeatedly inserted and removed while the structure remains in the tetragonal phase.[17,19−35] Because it does not contain a planar or linear channeled structure, however, fast ion intercalation is not observed in bulk versions of this material, but creating nanoscale versions of this material including nanocrystals and nanowires shows promise for improved kinetics.[15,19−32] One complication noted for $LiMn_2O_4$ (LMO) is that discharge rates can be much higher than charge rates, and for many applications, it is fast charging that is key to expanded use.[31−34] For the work presented here, all charge and discharge rates are the same, so that materials with fast kinetics should be useful for both high output power and fast charging applications.

The use of nanoparticles or wires alone does not solve the diffusion problem unless each individual nanoparticle or nanowire can be exposed to the liquid electrolyte. Nanocrystal-based nanoporous materials are one method that can be used to create this idealized architecture. These structures are generally made by templating methods where a hard (*e.g.*, silica[35]) or soft (*e.g.*, polymer[36]) template is intimately mixed with the material of interest, and then the template is selectively removed to produce the desired porous structure. Block copolymer templating of preformed nanocrystals is one method that has had much success in creating these nanostructures.[5,37−42] Prior to coassembly with the organic polymer, the ligands are stripped from the nanocrystals,[43] enabling the nanocrystals to loosely fuse together, forming the pore walls.[37,38] Because micropores are created at the intersections between nanocrystals, the electrolyte effectively penetrates into the pore wall, providing short diffusion lengths for Li^+ within single nanocrystalline grains. Electronic conduction then occurs through the interconnected walls of the mesoporous material. The short ion and electron path lengths should promote pseudocapacitive behavior in otherwise diffusion-controlled systems.

The primary difficulty in creating controlled nanoscale architectures from $LiMn_2O_4$ spinel is the fact that the compound is very difficult to produce in soluble form. Fortunately, a synthetic route to $LiMn_2O_4$ exists from the solid-state conversion reaction between Mn_3O_4 spinel and LiOH.[44−47] This is beneficial because there is a large body of literature aimed at making soluble transition metal oxide nanocrystals including Mn_3O_4.[48−64] Additionally, control over both size and composition is relatively easy for these transition metal oxide spinels.[48−64] The spinel nanocrystals can be ligand-stripped and coassembled with diblock copolymer templates to produce nanoporous networks with homogeneous nano-sized porosity.[38] The resulting nanoporous $LiMn_2O_4$ materials are useful as charge storage systems not only because of improved kinetics but also because size effects help alleviate various structural changes that contribute to a drop-off of cycling stability. Examples of such structural problems eased by nanostructure include Jahn−Teller distortion,[65] formation of two cubic phases,[66] loss of crystallinity,[67] and development of microstrain.[68]

Many of these problems can also be reduced by fabricating nonstoichiometric $LiMn_2O_4$.[17,65−67] $Li_xMn_2O_4$, where $x \geq 2$, is not a good choice for charge storage at high rates as lithiation at or beyond $x = 2$ causes a transformation of the spinel from cubic to tetragonal symmetry, which results in poor cycling reversibility.[16] $Li_xMn_2O_4$, where $x < 1$, is also not optimal as it suffers from reduced capacity. $Li_xMn_2O_4$, where $2 > x > 1$, however, seems to be the most promising direction as it allows for a material that does not change phase during cycling or suffer from capacity loss due to lithium depletion. Moreover, the nonstoichiometric nature actually helps solve some cycling problems.[67]

In this paper, we thus report on the development of a polymer templating route for fabricating nanoporous thin films of $Li_xMn_2O_4$ with $1 < x < 2$. These materials are designed as cathodes for lithium-ion-based pseudocapacitors and are ideal systems for studying charge/discharge kinetics. They are prepared by a solid-state conversion reaction between Mn_3O_4 nanocrystal-templated films and LiOH. The structural and electrochemical properties of nanoporous $Li_xMn_2O_4$ films are examined using a combination of high-angle X-ray diffraction (XRD), scanning electron microscopy (SEM), porosimetry, X-ray photoelectron spectroscopy (XPS), and a broad range of electrochemical studies. The results show that the films display pseudocapacitive behavior as a result of the extremely short diffusion lengths and mesoporous nature of the electrode material.

RESULTS

The fabrication of thin film nanoporous $Li_xMn_2O_4$ $(1 < x < 2)$ was achieved by nanocrystal templating of a precursor phase, followed by a solid-state conversion reaction. First, 7−8 nm Mn_3O_4 nanocrystals were synthesized in solution from a manganese(II) acetate precursor. These nanocrystals were then dissolved in solution with a block copolymer and dip-coated onto indium-doped tin oxide (ITO) substrates for electrochemical measurements or silicon substrates for structural characterization. The resulting films were calcined at 425 °C in air to remove the block copolymer template. A solution of $LiOH \cdot H_2O$ was spin-coated onto the nanoporous Mn_3O_4 films. The films were calcined again at 500 °C in air, resulting in nanoporous $Li_xMn_2O_4$ $(1 < x < 2)$ films. The structures of the nanoporous Mn_3O_4 and $LiMn_2O_4$ films were characterized using high-angle XRD, SEM, porosimetry, and XPS. For the electrochemical investigation, a three-electrode flooded cell was used with the nanoporous $Li_xMn_2O_4$ film as the working electrode, and Li foil was used for both the counter and reference electrodes. Cyclic voltammetry (CV) and galvanostatic analysis were both employed.

The crystalline phase of the initial Mn_3O_4 was determined using grazing incidence XRD. All peaks could be indexed to a single phase of cubic spinel Mn_3O_4 (Figure 1a). The broad peak widths indicate the nanocrystallinity of the structure. Using the Scherrer formula and a spherical shape factor, the crystallite size was calculated to be 8.4 nm. The mesoporous structure of the Mn_3O_4 can be seen from the SEM (Figure 1b); the sample has a wall thickness of 14.4 ± 2.9 nm based on over 100 measurements. This value is slightly larger than the calculated crystallite size, indicating that some walls are composed of multiple crystalline domains. Pore size was also measured from SEM images and determined to be 17.0 ± 6.4

DOI: 10.1021/acsnano.6b02608
ACS Nano 2016, 10, 7572−7581

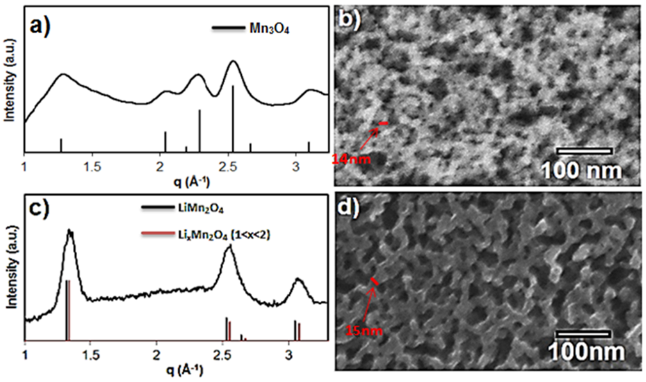

Figure 1. (a) XRD pattern and (b) SEM image from a nanoporous Mn_3O_4 film on a silicon wafer. (c) XRD pattern and (d) SEM image from a nanoporous $Li_xMn_2O_4$ ($1 < x < 2$) film on a silicon wafer.

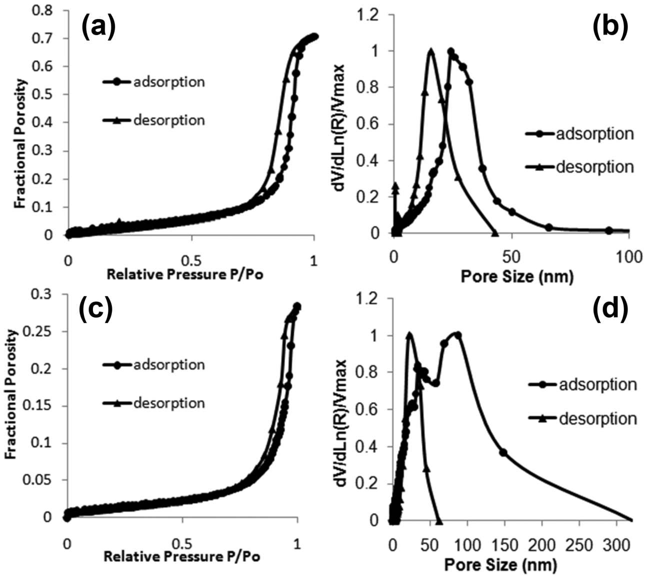

Figure 2. Adsorption and desorption isotherms (a,c) and Barrett−Joyner−Halenda (BJH) adsorption and desorption pore size distributions (b,d) for nanoporous Mn_3O_4 (a,b) and $Li_xMn_2O_4$ (c,d).

nm. This image analysis was then correlated with porosimetry (Figure 2a,b), which indicated that the structure was about 70% porous with an average cage size of 24 nm, calculated from the adsorption isotherm, and an average neck size of 15 nm, calculated from the desorption isotherm. It is expected that a top-view SEM should show some combinations of cages and necks in a random surface, so the SEM and porosimetry results are in good agreement.

XRD data of the post-conversion samples (Figure 1c) were indexed exclusively to an over-lithiated spinel $Li_xMn_2O_4$ (JCPDS: 00-051-1582) with a Li/Mn ratio of about 0.7:1. The JCPDS of pure $LiMn_2O_4$ (00-35-0782) is included in the figure for comparison. Note that excess lithium (when $1 < x < 2$ in $Li_xMn_2O_4$) does not change the spinel structure of the material. Only when $x \geq 2$ is a transformation to tetragonal $Li_2Mn_2O_4$ observed. It should also be noted that the tetragonal phase is generally reached by over-lithiating the $LiMn_2O_4$ structure by electrochemical insertion at the 3 V plateau.[69] Any excess lithium above $x = 1$ but less than $x = 2$ added before heat treatment results in the same cubic spinel as $LiMn_2O_4$ but shifts the peaks toward higher q (and 2θ) due to change in the lattice parameters. The peaks are once again broad due to the finite thickness of the walls in the porous structure, as indicated by a crystallite size of 13 nm calculated using the Scherrer equation. Slight wall thickness growth can be observed by SEM (Figure 1d) and was found to be 14.8 ± 3.8 nm based on over 100 measurements. Scherrer size calculated here is far closer to the measured value from SEM, indicating the formation of more single domain walls after conversion from Mn_3O_4 to $Li_xMn_2O_4$. The mesoporosity retained by the $Li_xMn_2O_4$ ($1 < x < 2$) film can also be seen by SEM, and average pore size based on more than 100 measurements was found to be 25 nm ±11 nm. Porosimetry (Figure 2c,d) indicated a retained porosity of about 30% for nanoporous $Li_xMn_2O_4$ films of various thicknesses (between 100 and 300 nm) with no presence of micropores. The fact that the pore fraction does not change with film thickness indicates that the mesopores are most likely interconnected throughout the entire thickness of the material. A somewhat broadened cage size distribution, calculated from the adsorption isotherm, ranges from 20 nm to slightly more than 100 nm with two size maxima at ∼30 and ∼100 nm. The 30 nm pores likely correspond to those observed by SEM, while the larger cages likely arise from regions of fused pores, which are not easy to directly quantify in a top-view SEM image. Pore fusion likely occurs during the solid-state transformation process from manganese oxide to lithium manganese oxide. The neck size calculated from the desorption isotherm was found to be 22 nm which combined with the smaller adsorption cage sizes at 30 nm nicely brackets the 25 nm average pore size calculated from SEM. The surface area of the mesoporous film was calculated to be 24 m^2/g based on a geometric model that assumes spherical pores with a size of 25 nm and a total porosity of 30%, as determined by toluene adsorption experiments (see Supporting Information for calculation details). We note that 25 nm is at the small end of our pore size estimates, making this an over-estimate of the real surface area.

The nanoporous $Li_xMn_2O_4$ ($1 < x < 2$) films deposited on the ITO substrates were used directly as working electrodes for determining electrochemical properties. Cyclic voltammetry measurements were made from 3.4 to 4.5 V (*vs* Li/Li^+) at various sweep rates ranging from 1 to 100 mV/s (Figure 3a,b). A linear baseline correction was used to offset an ohmic response of the electrolyte at high potentials. Two peaks are present during both lithium removal (anodic sweep) and insertion (cathodic sweep) for all sweep rates. The presence of two peaks is explained in the literature as arising from two slight lattice shifts within the spinel structure.[70] At the slower sweeps from 1 to 10 mV/s, the anodic peaks A1 and A2 are at 4.0 and 4.2 V, respectively, whereas the cathodic peaks C1 and C2 are at 3.9 and 4.1 V (Figure 3a). A1, which is coupled with C1, corresponds to the first 0.5 mol of lithium removed in $LiMn_2O_4$ and A2, which is coupled with C2, corresponds to the second 0.5 mol of lithium removal. The peaks correspond to 25 and 75% of lithium removed from stoichiometric $LiMn_2O_4$, which is where the lattice parameter shifts in the spinel.[70]

In stoichiometric $LiMn_2O_4$, the two anodic peaks correspond to the following reversible two-step process upon delithiation:[70]

$$\text{A1: } LiMn_2O_4 \rightarrow Li_{0.5}Mn_2O_4 + 0.5Li^+ + 0.5e^-$$
$$\text{(theoretical capacity 74 mAh/g)} \qquad (1)$$

DOI: 10.1021/acsnano.6b02608
ACS Nano 2016, 10, 7572−7581

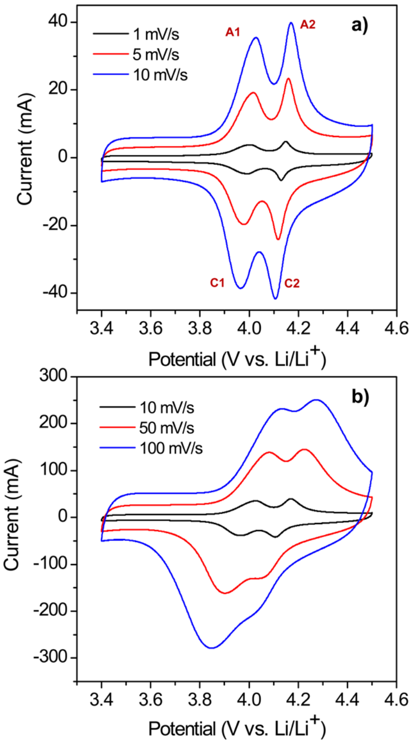

Figure 3. Cyclic voltammetry of a nanoporous of $Li_xMn_2O_4$ ($1 < x < 2$) film collected using a lithium counter and reference electrode, cycled between 3.4 and 4.5 V at sweep rates of (a) 1, 5, and 10 mV/s and (b) 10, 50, and 100 mV/s.

$$\text{A2: } Li_{0.5}Mn_2O_4 \rightarrow Mn_2O_4 + 0.5Li^+ + 0.5e^- \quad \text{(theoretical capacity 74 mAh/g)} \tag{2}$$

$$\text{A1 + A2: } LiMn_2O_4 \rightarrow Mn_2O_4 + Li^+ + e^- \quad \text{(theoretical capacity 148 mAh/g)} \tag{3}$$

The cathodic peaks correspond to the reverse processes. Since the peaks in Figure 3 are present at positions nearly identical to those reported for $LiMn_2O_4$ in the literature,[71−73] it is presumed that this same process occurs in the slightly over-lithiated $Li_xMn_2O_4$ ($1 < x < 2$).[17,65−67] However, the excess lithium above $x = 1$ can only be accessed at the 3 V plateau and therefore does not contribute to the 4 V capacity. Additionally, it has been suggested that superstoichiometric lithium helps support the spinel structure at the 4 V plateau, increasing cycle life.[16,20]

Our thin film nanoporous $Li_xMn_2O_4$ ($1 < x < 2$) showed significantly lower overall capacity, compared to the same material with larger grain size.[29,72−74] At a sweep rate of 1 mV/s (corresponding to a charging time of 20 min), a reversible capacity of 65 mAh/g is achieved, whereas that at 10 mV/s (corresponding to a charging time of 2 min) is 55 mAh/g. Although the theoretical capacity of $LiMn_2O_4$ is 148 mAh/g, less than half of that value is observed in our materials even at slow scan rates. This reduced capacity is not due to electrolyte inaccessibility to the pores, as films between 100 and 300 nm thick showed the same kinetics and mass-normalized capacity, indicating that the mesopores are interconnected within the $Li_xMn_2O_4$ structure and solvent can efficiently access all parts of the porous film. Similar capacity decreases have been observed previously in $LiMn_2O_4$, as well as other similar nanocrystalline cathode systems, such as $LiCoO_2$ below a certain grain size, and are discussed below.[15,20,75]

To understand the capacity loss, we first examine the CV curves. Nanostructured $LiMn_2O_4$ retains the distinctive double peak structure and the same peak positions as bulk $LiMn_2O_4$.[20] This suggests that the same physical processes are occurring in both the nanoscale and bulk materials.[70] One possible explanation for the capacity reduction in certain nanostructured materials is discussed by Okubo *et al.*[15] In this paper, the authors discuss how $LiCoO_2$, which normally has cobalt in the +3 oxidation state, has lower oxidation state Co^{2+} on the surface. Because the transition at the 3.5 V plateau in $LiCoO_2$ is Co^{3+} to Co^{4+}, these surface Co^{2+} sites cannot be oxidized electrochemically at these high voltages. With decreasing crystallite size and increasing surface area in the material, a point is reached where Co^{2+} constitutes a significant fraction of the total cobalt in the system, thus reducing the capacity. Similar effects have been shown to occur in $LiMn_2O_4$. Recent work using high-angle annular dark-field scanning transmission electron microscopy images of the surface of $LiMn_2O_4$ (which should contain exclusively $Mn^{3/4+}$) revealed a spinel structure with reduced Mn^{2+} in the tetrahedral sites rather than the expected Li^+.[76] The paper indexes this surface phase of $LiMn_2O_4$ as Mn_3O_4, which would be unable to undergo a $Mn^{3+} \rightarrow Mn^{4+}$ transition and thus would be inactive at potentials relevant to this system, similar to the $LiCoO_2$. These results are also supported by simulations in the literature, which have shown that the surface of $LiMn_2O_4$ is only stable when reduced compared to bulk.[77,78] An interesting feature of this mechanism for capacity loss is that it explains why the same redox processes are observed in bulk and nanoscale materials, but a portion of the structure is not accessible for redox reactions at the expected voltage.

To understand if this phenomenon is occurring in our system, XPS was collected on a pristine nanoporous $Li_xMn_2O_4$ ($1 < x < 2$) thin film (Figure 4a). The data reveal that about 40% of the manganese present on the material surface is in the +2 oxidation state. As discussed above, because the 4 V plateau is associated with oxidation of Mn^{3+} to Mn^{4+}, this reduced Mn^{2+} should reduce surface capacity.[70] To confirm this idea, XPS was also collected on a sample after plasma etching (Figure 4b), which was used to remove the majority of the surface layer. In this case, the data show that only 10% of the manganese present is in the +2 oxidation state. This shows that the Mn^{2+} is concentrated on the surface, and these reduced surface atoms are likely the cause of the reduced capacity in this nanostructured material.

Galvanostatic cycling was also used to study capacity and capacity fade during repetitive charge−discharge cycles. Galvanostatic discharge curves (Figure 5a) show continuously sloping voltages during lithium intercalation and deintercalation rather than plateaus at distinct voltages, which occurs with bulk and larger crystallite systems.[15,20−36] These sloping voltage profiles are considered one of the hallmarks of pseudocapacitive behavior.[1] At a rate of 50C, this material stores approximately 0.3 mol of lithium per mole of $Li_xMn_2O_4$ ($1 < x < 2$), corresponding to a capacity of around 44 mAh/g. The decrease in capacity with increasing *C* rate is consistent with the cyclic voltammetric results, and even at 1000C, this material can still reversibly store approximately 20 mAh/g, corresponding to 0.1 mol of lithium per mole of $Li_xMn_2O_4$ ($1 < x < 2$). It should be noted that, at these very fast rates, ohmic polarization may contribute to capacity loss because of the flooded half-cell

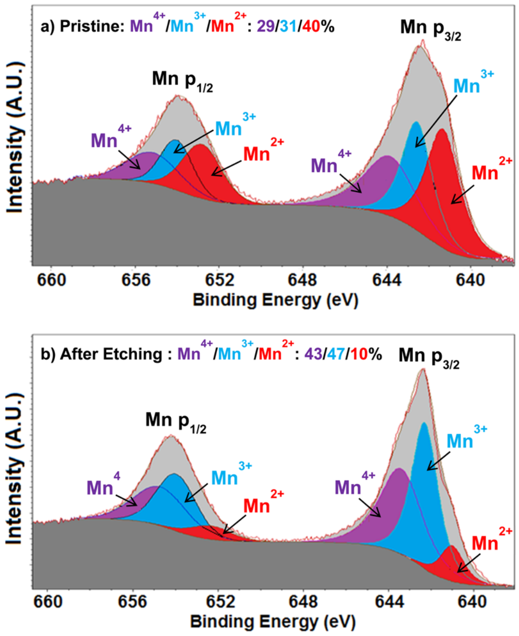

Figure 4. X-ray photoelectron spectra of Mn 2p core levels for $Li_xMn_2O_4$ ($1 < x < 2$) mesoporous thin films (a) before plasma etching and (b) after plasma etching. Fitting was done using CasaXPS software with Gaussian/Lorentzian 75/25 for Mn $p_{3/2}$ and 30/70 for Mn $p_{1/2}$ peaks.

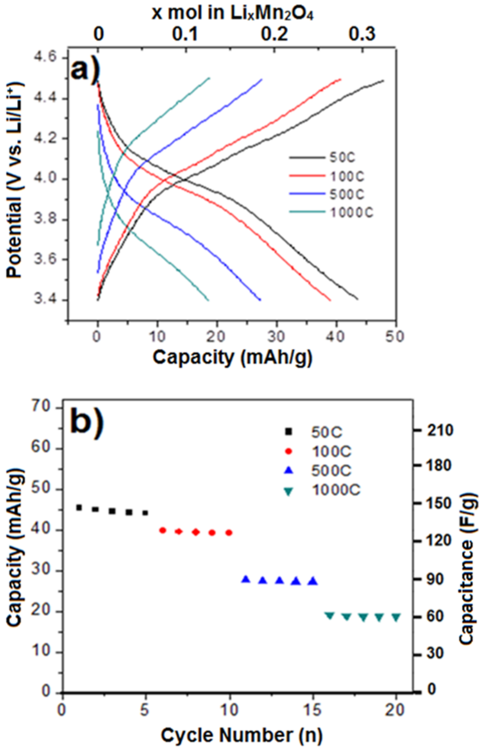

Figure 5. (a) Galvanostatic charge and discharge curves for nanoporous $Li_xMn_2O_4$ at various rates (50C, 100C, 500C, 1000C), which correspond to current densities of 3.3, 6.5, 32, and 65 A/g, respectively. (b) Discharge capacity *versus* cycle number at the same four rates. Samples were charged and discharged at the same rate.

geometry used in this work. As a result, capacity values at very high current densities should be considered as a lower limit on the intrinsic capacity of the material. Long-term galvanostatic cycling (Supporting Information Figure S1) further shows that, at a C rate of 32C, this material retains 90% of its initial capacity after 265 cycles.

It should be additionally noted that the majority of the capacity is not the result of electric double-layer capacity. Assuming a value of 10 $\mu F/cm^2$ (a typical double-layer capacitance[79]) and specific surface area of 24 m^2/g, the electric double-layer capacity of the nanoporous $Li_xMn_2O_4$ ($1 < x < 2$) is only 0.7 mAh/g. This value is negligible compared to the measured capacity of 50–65 mAh/g. Therefore, the vast majority of capacity in these materials can be attributed to redox processes.

DISCUSSION

The 30% porosity of the nanoporous $Li_xMn_2O_4$ ($1 < x < 2$) and small wall thickness of ∼15 nm means that the porous materials presented here have both good pathways for electrolyte penetration throughout the mesoporous electrode structure and high internal surface area enabling the electrolyte to have complete access to the cathode material. The small wall thickness ensures that the majority of the lithium in this material is located in "near-surface" sites. Here, we define near-surface sites to be those interior sites that can be kinetically accessed on very short time scales because of short diffusion lengths. We note that true surface redox is likely not available in these materials in this voltage range because of the reduced, inactive surface, as discussed above. While we would not expect the cubic $Li_xMn_2O_4$ spinel to show particularly fast lithium-ion diffusion rates, the 15 nm wall thickness represents a very short diffusion length that enables the rapid transport of significant amounts of lithium into the lithium manganese oxide framework.

The simplest indication that nanoporous $Li_xMn_2O_4$ ($1 < x < 2$) represents a viable pseudocapacitive cathode material comes from the retention of well-defined redox peaks at fast sweep rates (Figure 3). A second indication, also visible in Figure 3, is the voltage offset between the cathodic (C) and anodic (A) peaks. For the coupled C1–A1 and C2–A2 peaks, the degree of reversibility can be quantified by the separation between peak anodic and cathodic potentials ($\Delta E_p = E_{pa} - E_{pc}$).[80] This separation is a measure of the rate of electron transfer at the electrode surface.[80] For an electrochemically reversible process, $\Delta E_p \approx 0.059/n$, where n is the number of electrons transferred in the electrode reaction. Figure 6 illustrates that up to 10 mV/

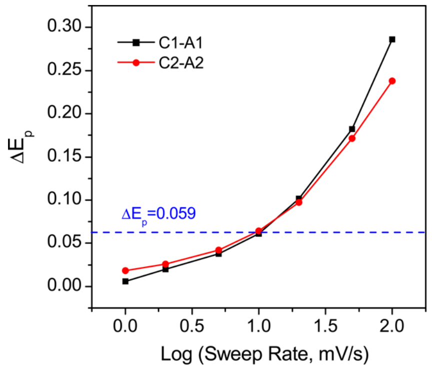

Figure 6. ΔE_p *versus* log of the sweep rate for nanoporous $Li_xMn_2O_4$ ($1 < x < 2$), showing the degree of reversibility at various sweep rates.

DOI: 10.1021/acsnano.6b02608
ACS Nano 2016, 10, 7572–7581

s, the electron transfer reaction is highly reversible, showing a $\Delta E_p \leq 0.059$. Such electrochemical reversibility suggests there is relatively little structural change upon lithiation and delithiation. This feature is important because structural change can lead to degradation of the electrode over time, and so a more stable structure can lead to a longer cycling lifetime. At rates above 10 mV/s, the process shows a greater degree of irreversibility, with a corresponding peak shift of the anodic peak to more positive potentials and the cathodic peak to more negative potentials occurs.[81] This implies that, at higher rates, higher over-potentials are necessary to deliver higher currents.

In order to gain greater insight into the reaction kinetics, the rate-limiting mechanisms for this material at both coupled redox peaks were investigated. We assume that the current, *i*, obeys a power-law relationship to the sweep rate, given by[82]

$$i = a\nu^b$$

where *a* is a constant and ν is the sweep rate. A *b* value of 0.5 indicates current that is limited by semi-infinite linear diffusion, and a *b* value of 1 indicates current that is not diffusion-limited. The latter includes the electrical double-layer contribution as well as pseudocapacitive processes. As mentioned previously, the electric double-layer capacity of the nanoporous $Li_xMn_2O_4$ ($1 < x < 2$) was calculated to be only 0.7 mAh/g, a negligible amount compared to the overall capacity attained from this material.[79] Based on this analysis, we attribute the majority of the charge storage, which is characterized by $b \sim 1$, to arise from pseudocapacitive mechanisms and not from electrical double-layer processes.

Figure 7 shows a plot of log peak current *versus* log sweep rate that was used to calculate the *b* values for the lower potential redox peaks (3.9 and 4.1 V), which are associated with Li^+-ion intercalation.[70−73] For charge times up to 110 s (10 mV/s), the *b* values are 1.0 or nearly so. This indicates capacitor-like behavior for lithium insertion/extraction for charge/discharge times of up to 2 min. At charge times shorter than 110 s, the *b* value drops to 0.86 and 0.69 for the 3.9 and 4.1 V redox peaks, respectively. These values signal the onset of diffusion-controlled kinetics for charge/discharge times of less than 2 min.

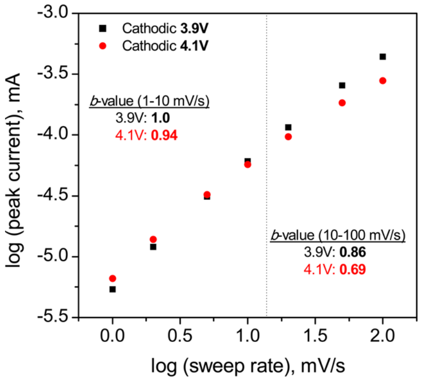

Figure 7. Plots of log(peak current) *vs* log(sweep rate) used to obtain *b*-values for the 3.9 and 4.1 V redox peaks.

In a complementary analysis, the current contribution *i* from the power-law relationship can be separated into two functions that describe capacitive (weighted by k_1) and diffusion-limited (weighted by k_2) processes as a function of potential:

$$i = k_1\nu + k_2\nu^{1/2}$$

Figure 8 illustrates how the diffusion-limited and capacitive processes are distributed over the potential range investigated.

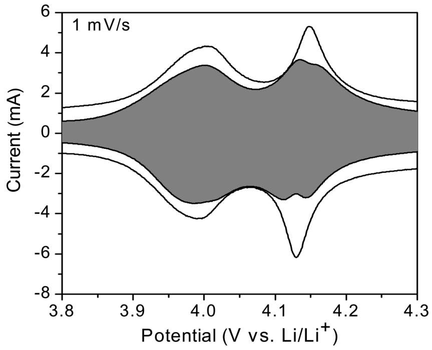

Figure 8. Capacitive contributions to the total current for nanoporous $Li_xMn_2O_4$ ($1 < x < 2$) at 1 mV/s. The current is 72% pseudocapacitive (shaded region).

The data were taken at the slow sweep rate of 1 mV/s to allow a diffusion-controlled process to contribute to the total current. Despite this fact, the material is 75% capacitive, with only 25% of the stored charge coming from diffusion-controlled processes. As expected, the potentials where more diffusion-controlled currents arise are associated with the redox peaks.

High levels of capacitive energy storage generally result when diffusion rates are fast and diffusion distances are short. It is thus worth considering if diffusion distance or rate is predominantly responsible for the favorable kinetics in this material. We have thus calculated diffusion constants for each redox peak from CV using the Randles−Sevcik equation (see Supporting Information Figure S2 and caption). The specific values are included in the Supporting Information, but all diffusion constants determined for all peaks, both anodic and cathodic, are $\sim 2 \times 10^{-11}$ cm^2/s. These values are in good agreement with previous measurements on bulk $LiMn_2O_4$.[83,84] Interestingly, the first reaction (A1 and C1) shows slightly slower kinetics than reaction 2 (A2 and C2). This is good agreement with the fact that the *b* value for reaction 1 is slightly lower (less capacitive) than that for reaction 2, as shown in Figure 6. Overall, this indicates that shorter diffusion pathways, rather than a change in the diffusion constant, are most likely the source of increased kinetics and the high fraction of capacitive current observed in this system.

Nanoporous $Li_xMn_2O_4$ ($1 < x < 2$) films with small wall thickness thus exhibit a number of pseudocapacitive characteristics. The existence of $b = 1$ for reasonably high charge/discharge times, the small voltage offset between redox peaks, and the absence of any structural change upon lithiation and delithiation are all consistent with pseudocapacitor behavior. However, there are other features which are inconsistent with a classic capacitive response; the CV is not a "box", and while the decrease in voltage in the galvanostatic experiments has substantial linearity (Figure 5a), there is evidence of a shoulder that is not consistent with classic capacitive behavior.

Because the $LiMn_2O_4$ system has been well-studied, there is the opportunity to compare thin film mesoporous materials with previous studies of both bulk and nanoscale materials. Micron-sized particles of $LiMn_2O_4$ exhibit significantly reduced capacity at faster charge/discharge times.[29,30] For example, Kiani *et al.*[29] showed that micron-sized powders charged in 30

DOI: 10.1021/acsnano.6b02608
ACS Nano 2016, 10, 7572−7581

min (2*C*) deliver a capacity of 40 mAh/g, whereas nano-sized powders gave this capacity with 4 min of charge (15*C*). By comparison, our system achieves 40 mAh/g charging and discharging in 36 s (100*C*) in the same potential range. One complication for LMO is that the material can show very high discharge rates but requires charge at a significantly lower rate.[31−34] Consider, for example, work on 4 nm $Li_xMn_2O_4$ nanowires. Lee *et al.*[31] reported that after charging for 1 h (1*C*) followed by discharge in 2 min (30*C*), their material exhibited 50% capacity retention, but no 30*C* charge data were included. This same behavior of fast discharge is also observed for nanocrystal systems. Shaju and Bruce show that ∼50 nm sized $LiMn_2O_4$ powders show nearly 90% capacity retention after 1000 cycles using *C*/2 charge times and 10*C* discharge times, further supporting the idea that discharge kinetics are linked to size in $LiMn_2O_4$ systems.[32] To achieve fast charge times, as well, however, smaller structures are needed. For the system presented here, 50% capacity retention is achieved with both charge and discharge at 100*C* (Figure 5a).

Although the overall charge storage capacities are not terribly high, the rate behavior and cycle life for nanoporous $Li_xMn_2O_4$ ($1 < x < 2$) is very good. Moreover, the ability to charge ∼50 mAh/g in 1 min (Figure 9) makes this material interesting for high-rate charge storage devices. Additionally, nanoporous $Li_xMn_2O_4$ has the distinction of being the first cathode material to exhibit pseudocapacitive charge storage above 4 V. Finally, because $Li_xMn_2O_4$ ($1 < x < 2$) is just one member of a large family of related spinel structured lithium transition metal oxide materials, there is opportunity to optimize and improve kinetics, the stability, and even the potential range of similar nanostructured materials.[85,86]

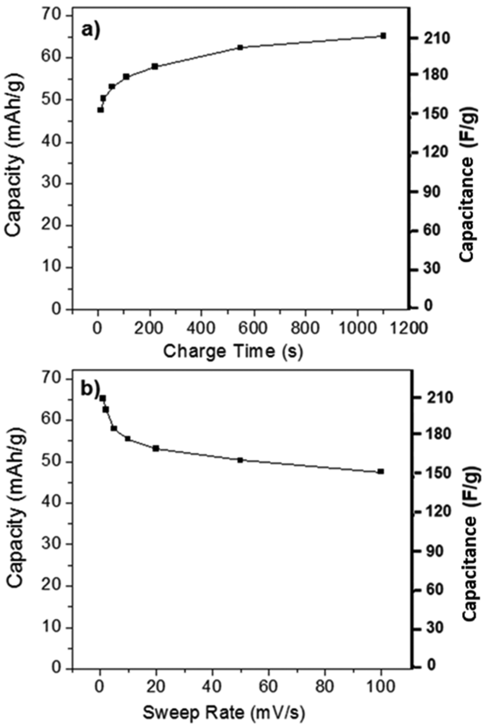

Figure 9. Rate dependence of the discharge capacity for nanoporous $Li_xMn_2O_4$ ($1 < x < 2$) as a function of charge time (a) and sweep rate (b). Samples were charged and discharged at the same rate.

CONCLUSION

Nanoporous thin films of the cathode material $Li_xMn_2O_4$ ($1 < x < 2$) were prepared by solid-state conversion in which a nanoporous Mn_3O_4 thin film was reacted with LiOH. The resulting thin films with 30% porosity and a wall thickness of ∼15 nm were characterized using both potentiostatic and galvanostatic cycling to determine their charge storage properties. The reversible lithium-ion capacities were significantly less than theoretical values likely due to over-expression of low oxidation state Mn defects on the surface which are electrochemically inactive at high voltage, an effect seen in other nanostructured cathode systems.[15,20] Despite the inactive surface, the small voltage offset in peak potentials at sweep rates up to 10 mV/s, combined with *b* values close to 1, further indicates that these materials show capacitor-like kinetics. Indeed, kinetic analysis indicates that some 75% of the charge storage is associated with capacitive behavior. The predominance of fast, reversible redox reactions in nanoporous $Li_xMn_2O_4$ ($1 < x < 2$) is attributed to the direct access of the electrolyte through the mesopores in combination with the short diffusion path lengths, which stem from the small wall thickness in these porous materials. Moreover, the small wall thickness allows for both fast charge and fast discharge; while fast discharge is common in nanostructured cathode materials, fast charging is not usually observed. These results thus demonstrate that nanoporous $Li_xMn_2O_4$ ($1 < x < 2$) can behave as a pseudocapacitive cathode material with exciting potential for application in high-rate, asymmetric energy storage devices.

EXPERIMENTAL SECTION

Materials. The following chemicals were purchased and used as received: oleylamine (90% Aldrich), stearic acid (95%, Aldrich), xylene (98%, Aldrich), manganese(II) acetate (98%, Aldrich). Poly(butylene oxide)-*b*-poly(ethylene oxide), with a mass ratio of PBO(5000)-*b*-PEO(6500), a block ratio PBO90-*b*- PEO114, and with a PDI = 1.09, was purchased from Advanced Polymer Materials. Lithium hydroxide monohydrate reagent grade crystals were purchased from Acros Organics.

Synthesis and Ligand Exchange of Mn_3O_4 Nanocrystals. A previously reported procedure was followed to synthesize 4−5 nm Mn_3O_4 nanocrystals stabilized by oleylamine ligands.[23,49] Briefly, 0.17 g manganese(II) acetate, 0.57 g of stearic acid, and 3.2 mL of oleylamine were dissolved in 15 mL of xylene and stirred at 90 °C for 3 h in air to produce Mn_3O_4 nanocrystals. Mn_3O_4 nanocrystals were washed several times with ethanol before being dispersed in hexane (10−15 mg/mL). To remove the surface-passivating ligands, Mn_3O_4 nanocrystals were treated with $NOBF_4$ according to a previously reported procedure.[23,43] In a typical ligand-exchange reaction, 5 mL of nanocrystal dispersion in hexane was combined with 5 mL of $NOBF_4$ solution in *N*,*N*-dimethylformamide (DMF) (10 mg/mL) with stirring (5 min) or until the nanocrystals were transferred to the DMF phase. The nanocrystals were precipitated with toluene and centrifuged, followed by multiple washings with DMF/toluene and ethanol. The ligand-stripped nanocrystals were dispersed in DMF/ethanol (1:5 v/v) to give a final concentration of 15−20 mg/mL.

Synthesis of Mesoporous Mn_3O_4 Films. Films were prepared in a manner similar to previous reports.[23] In a typical synthesis, 40 mg of poly(butylene oxide)-*b*-poly(ethylene oxide) was dissolved in 0.5 mL of ethanol with gentle heating. To this solution, we added 3 mL of the ligand-free Mn_3O_4 in DMF/ethanol (15−20 mg/mL). From this mixture, thin films were dip-coated onto clean, polar substrates (silicon or ITO) at a constant withdrawal rate of 1−10 mm/s with a constant 30% relative humidity. Thermal decomposition of the template was done by a 12 h ramp to 425 °C in air.

Conversion of Mn_3O_4 to $Li_xMn_2O_4$ Mesoporous Films. Conversion reactions were performed by spin-drying 9.0 μL/cm^2 of a 0.25–0.75 mg/mL LiOH·H_2O solution in ethanol (concentration depends on the film thickness) onto mesoporous Mn_3O_4 thin films ranging in thickness from 100 to 300 nm. The term "spin-drying" is used to denote a process where an aliquot of solution is spread over a porous sample by slow spin-coating and then allowed to dry. All films were thermally converted to nanoporous $Li_xMn_2O_4$ using a 2 h ramp to 500 °C in air, followed by a 2 h soak at 500 °C. To optimize the amount of LiOH·H_2O used during synthesis, nanoporous Mn_3O_4 films were dosed with different amounts of LiOH and heated at 500 °C to yield various stoichiometries of $Li_xMn_2O_4$. Samples were then electrochemically cycled to determine which materials showed the characteristic electrochemistry of $LiMn_2O_4$. Promising samples were then fully digested, and atomic composition was investigated using inductive coupled plasma atomic emission spectroscopy to determine Li and Mn content. Samples with the highest capacities and with electrochemical characteristics indicative of $LiMn_2O_4$ were all found to be in the range of $1 < x < 2$ for nanoporous $Li_xMn_2O_4$ thin films.

Characterization of Mn_3O_4 and $Li_xMn_2O_4$ Mesoporous Films. XRD was taken using both synchrotron high-angle XRD carried out on beamline 11-3 at the Stanford Synchrotron Radiation Laboratory as well as in-house on a Panalytical X'Pert Pro X-ray powder diffractometer using a Bragg–Brentano setup. Scherrer widths were calculated and corrected using peak broadening parameters specific to the instrument setup used: Debye–Scherrer and Bragg–Brentano for synchrotron and panalytical instruments, respectively. SEM images were obtained using a JEOL JSM-6700F field emission electron microscope with 5 kV accelerating voltage and secondary electron detector configuration. More than 100 measurements were taken using ImageJ to obtain the average wall thickness and pore size of the nanoporous Mn_3O_4 and $Li_xMn_2O_4$ thin films. Thin film porosimetry on both nanoporous Mn_3O_4 and $Li_xMn_2O_4$ films made use of a Sopra model GES5E elipsometric porosimeter using toluene as the adsorbant. Data were analyzed by Spectroscopic Elipsometry Analyzer version 1.4.56. XPS was taken using a Kratos XPS Axis Ultra DLD spectrometer with a monochromatic Al (Kα) radiation source. Fitting was done using CasaXPS software with Gaussian/Lorentzian 75/25 for Mn $p_{3/2}$ and 30/70 for Mn $p_{1/2}$ peaks. The samples were etched with an Ar beam (raster size 5 mm × 5 mm) for 1 min. To determine the sample mass, samples were fully dissolved in 1 mL each of concentrated ICP-grade HCl and HNO_3 at room temperature, and the dissolved solutions were then analyzed for total Mn and Li content using inductively coupled plasma optical emission spectroscopy (ICP-OES). A Varian 720-ES ICP-OES was used to assess the manganese and lithium content, which was used to calculate both the stoichiometry and the active mass of $Li_xMn_2O_4$.

Electrochemical Analysis. All electrochemical experiments were made in an argon-filled glovebox with oxygen and moisture levels less than 1 ppm. Electrochemical measurements were carried out in a three-electrode cell using a BIOLOGIC VMP-3 potentiostat. The working electrode consisted of nanoporous $Li_xMn_2O_4$ films coated onto ITO glass. The electrolyte solution used was 1.0 M $LiClO_4$ in propylene carbonate, and lithium metal was used as both the counter and reference electrodes. Cutoff voltages at 4.5 and 3.4 V *vs* Li/Li^+ were used for cyclic voltammetry and galvanostatic cycling. The active mass was calculated using ICP-OES, as described above.

ASSOCIATED CONTENT

S Supporting Information

The Supporting Information is available free of charge on the ACS Publications website at DOI: 10.1021/acsnano.6b02608.

> Calculations for specific surface area, long-term cycling data for nanoporous $Li_xMn_2O_4$ films, and calculation of Li^+ diffusion constants (PDF)

AUTHOR INFORMATION

Corresponding Authors

*E-mail: tolbert@chem.ucla.edu.
*E-mail: bdunn@ucla.edu.

Notes

The authors declare no competing financial interest.

ACKNOWLEDGMENTS

This work was initiated as part of the Center for Molecularly Engineered Energy Materials (MEEM), an Energy Frontier Research Center funded by the U.S. Department of Energy (DOE), Office of Science, Office of Basic Energy Sciences, under Award DE-SC001342 (S.T. and B.D.). The work was continued and completed as part of DOE Grant DE-SC0014213 (S.T.). DOE funded efforts includes experimental design, materials synthesis, materials characterization, and some electrochemical measurements. Additional support for electrochemical measurements and analysis was provided by the Office of Naval Research (J.K and B.D.). The XPS instrument used in this work was obtained with support from the National Science Foundation, Award Number 0840531. Use of the Stanford Synchrotron Radiation Lightsource, SLAC National Accelerator Laboratory, is supported by the U.S. Department of Energy, Office of Science, Office of Basic Energy Sciences under Contract No. DE-AC02-76SF00515.

REFERENCES

(1) Simon, P.; Gogotsi, Y.; Dunn, B. Where Do Batteries End and Supercapacitors Begin? *Science* **2014**, *343* (6176), 1210–1211.

(2) Brezesinski, T.; Wang, J.; Tolbert, S. H.; Dunn, B. Ordered Mesoporous Alpha-MoO_3 with Iso-Oriented Nanocrystalline Walls for Thin-Film Pseudocapacitors. *Nat. Mater.* **2010**, *9*, 146–151.

(3) Augustyn, V.; Come, J.; Lowe, M.; Kim, J.; Taberna, P.; Tolbert, S. H.; Abruña, H.; Simon, P.; Dunn, B. High-Rate Electrochemical Energy Storage Through Li+ Intercalation Pseudocapacitance. *Nat. Mater.* **2013**, *12*, 518–522.

(4) Brezesinski, K.; Wang, J.; Haetge, J.; Reitz, C.; Steinmueller, S. O.; Tolbert, S. H.; Smarsly, B. M.; Dunn, B.; Brezesinski, T. Pseudocapacitive Contributions to Charge Storage in Highly Ordered Mesoporous Group V Transition Metal Oxides with Iso-Oriented Layered Nanocrystalline Domains. *J. Am. Chem. Soc.* **2010**, *132*, 6982–6990.

(5) Rauda, I. E.; Augustyn, V.; Saldarriaga-Lopez, L. C.; Chen, X.; Schelhas, L. T.; Rubloff, G. W.; Dunn, B.; Tolbert, S. H. Nanostructured Pseudocapacitors Based on Atomic Layer Deposition of V_2O_5 onto Conductive Nanocrystal-Based Mesoporous ITO Scaffold. *Adv. Funct. Mater.* **2014**, *24*, 6717.

(6) Kaskhedikar, N. A.; Maier, J. Lithium Storage in Carbon Nanostructures. *Adv. Mater.* **2009**, *21*, 2664–2680.

(7) Takami, N.; Satoh, A.; Hara, M.; Ohsaki, T. Structural and Kinetic Characterization of Lithium Intercalation into Carbon Anodes for Secondary Lithium Batteries. *J. Electrochem. Soc.* **1995**, *142*, 371–379.

(8) Guyomard, D.; Tarascon, J. M.; Li, J. Metal-Free Rechargeable $LiMn_2O_4$/Carbon Cells: Their Understanding and Optimization. *J. Electrochem. Soc.* **1992**, *139*, 937–948.

(9) Hwang, H.; Kim, H.; Cho, J. MoS_2 Nanoplates Consisting of Disordered Graphene-Like Layers for High Rate Lithium Battery Anode Materials. *Nano Lett.* **2011**, *11*, 4826–4830.

(10) Xiao, J.; Choi, D.; Cosimbescu, L.; Koech, P.; Liu, J.; Lemmon, J. P. Exfoliated MoS_2 Nanocomposite as an Anode Material for Lithium Ion Batteries. *Chem. Mater.* **2010**, *22*, 4522–4524.

(11) Soon, J. M.; Loh, K. P. Electrochemical Double-Layer Capacitance of MoS_2 Nanowall Films. *Electrochem. Solid-State Lett.* **2007**, *10*, A250–A254.

(12) Du, G.; Guo, Z.; Wang, S.; Zeng, R.; Chen, Z.; Liu, H. Superior Stability and High Capacity of Restacked Molybdenum Disulfide as Anode Material for Lithium Ion Batteries. *Chem. Commun.* **2010**, *46*, 1106–1108.

(13) Wei, M.; Wei, K.; Ichihara, M.; Zhou, H. Nb_2O_5 nanobelts: A Lithium Intercalation Host with Large Capacity and High Rate Capability. *Electrochem. Commun.* **2008**, *10*, 980−983.

(14) Liu, C.; Zhou, F.; Ozolins, V. *First Principles Study for Lithium Intercalation and Diffusion Behavior in Orthorhombic Nb_2O_5 Electrochemical Supercapacitor*; American Physical Society Meeting February 27−March 2, 2012, abstract #B26.003.

(15) Okubo, M.; Hosono, E.; Kim, J.; Enomoto, M.; Kojima, N.; Kudo, T.; Zhou, H.; Honma, I. Nanosize Effect on High-Rate Li-Ion Intercalation in $LiCoO_2$ Electrode. *J. Am. Chem. Soc.* **2007**, *129*, 7444−7452.

(16) Wu, S.; Yu, M. Preparation and Characterization of *o*-$LiMnO_2$ Cathode Materials. *J. Power Sources* **2007**, *165*, 660−665.

(17) Thackeray, M. M. Structural Considerations of Layered and Spinel Lithiated Oxides for Lithium Ion Batteries. *J. Electrochem. Soc.* **1995**, *142*, 2558−2563.

(18) Mizushima, K.; Jones, P. C.; Wiseman, P. J.; Goodenough, J. B. Li_xCoO_2 (0 < x<-1): A New Cathode Material for Batteries of High Energy Density. *Mater. Res. Bull.* **1980**, *15*, 783−789.

(19) Xia, H.; Luo, Z.; Xie, J. Nanostructured $LiMn_2O_4$ and Their Composites As High-performance Cathodes for Lithium-Ion Batteries. *Prog. Nat. Sci.* **2012**, *22* (6), 572−584.

(20) Okubo, M.; Mizuno, Y.; Yamada, H.; Kim, J.; Hosono, E.; Zhou, H.; Kudo, T.; Honma, I. Fast Li-Ion Insertion into Nanosized $LiMn_2O_4$ without Domain Boundaries. *ACS Nano* **2010**, *4*, 741−752.

(21) Luo, J.; Wang, Y.; Xiong, H.; Xia, Y. Ordered Mesoporous Spinel $LiMn_2O_4$ by a Soft-Chemical Process as a Cathode Material for Lithium-Ion Batteries. *Chem. Mater.* **2007**, *19*, 4791−4795.

(22) Ju, S. H.; Kim, D. Y.; Jo, E. B.; Kang, Y. C. $LiMn_2O_4$ Powders Made from Nano-Sized Manganese Oxide Powders. *J. Ceram. Soc. Jpn.* **2007**, *115* (4), 241−244.

(23) Hwang, B.; Kim, S.; Lee, Y.; Han, B.; Kim, S.; Kim, W.; Park, K. Mesoporous Spinel $LiMn_2O_4$ Nanomaterial as a Cathode for High-Performance Lithium Ion Batteries. *Int. J. Electrochem. Sci.* **2013**, *8*, 9449−9458.

(24) Sassin, M. B.; Greenbaum, S. G.; Stallworth, P. E.; Mansour, A. N.; Hahn, B. P.; Pettigrew, K. A.; Rolison, D. R.; Long, J. W. Achieving Electrochemical Capacitor Functionality from Nanoscale $LiMn_2O_4$ Coatings on 3-D Carbon Nanoarchitectures. *J. Mater. Chem. A* **2013**, *1*, 2431−2440.

(25) Jayaraman, S.; Aravindan, V.; Kumar, P. S.; Ling, W. C.; Ramakrishna, S.; Madhavi, S. Synthesis of Porous $LiMn_2O_4$ Hollow Nanofibers by Electrospinning with Extraordinary Lithium Storage Properties. *Chem. Commun.* **2013**, *49*, 6677.

(26) Tang, W.; Hou, Y.; Wang, F.; Liu, L.; Wu, Y.; Zhu, K. $LiMn_2O_4$ Nanotube as Cathode Material of Second-Level Charge Capability for Aqueous Rechargeable Batteries. *Nano Lett.* **2013**, *13*, 2036−2040.

(27) Lee, M.; Lee, S.; Oh, P.; Kim, Y.; Cho, J. High Performance $LiMn_2O_4$ Cathode Materials Grown with Epitaxial Layered Nanostructure for Li-Ion Batteries. *Nano Lett.* **2014**, *14*, 993.

(28) Potapenko, A. V.; Chernukhin, S. I.; Kirillov, S. A. A New Method of Pretreatment of Lithium Manganese Spinels and High-Rate Electrochemical Performance of $Li[Li_{0.033}Mn_{1.967}]O_4$. *Mater. Renew Sustain Energy* **2015**, *4*, 40−44.

(29) Kiani, M. A.; Mousavi, M. F.; Rahmanifar, M. S. Synthesis of Nano- and Micro-Particles of $LiMn_2O_4$: Electrochemical Investigation and Assessment as a Cathode in Li Battery. Int. *Int. J. Electrochem. Sci.* **2011**, *6*, 2581−2595.

(30) Qu, Q. T.; Wang, G. J.; Liu, L. L.; Tian, S.; Shi, Y.; Wu, Y. P. Excellent Electrochemical Behavior of $LiMn_2O_4$ in Aqueous Electrolyte. *Funct. Mater. Lett.* **2010**, *3*, 151.

(31) Lee, H.; Muralidharan, P.; Ruffo, R.; Mari, C. M.; Cui, Y.; Kim, D. K. Ultrathin Spinel $LiMn_2O_4$ Nanowires as High Power Cathode Materials for Li-Ion Batteries. *Nano Lett.* **2010**, *10*, 3852−3856.

(32) Shaju, K. M.; Bruce, P. G. A Stoichiometric Nano-$LiMn_2O_4$ Spinel Electrode Exhibiting High Power and Stable Cycling. *Chem. Mater.* **2008**, *20*, 5557−5562.

(33) Tang, W.; Wang, X. J.; Hou, Y. Y.; Li, L. L.; Sun, H.; Zhu, Y. S.; Bai, Y.; Wu, Y. P.; Zhu, K.; van Ree, T. Nano $LiMn_2O_4$ as Cathode Material of High Rate Capability for Lithium Ion Batteries. *J. Power Sources* **2012**, *198*, 308−311.

(34) Jiang, H.; Fu, Y.; Hu, Y.; Yan, C.; Zhang, L.; Lee, P. S.; Li, C. Hollow $LiMn_2O_4$ Nanocones as Superior Cathode Materials for Lithium-Ion Batteries with Enhanced Power and Cycle Performances. *Small* **2014**, *10*, 1096−1100.

(35) Jiao, F.; Bao, J.; Hill, A. H.; Bruce, P. G. Synthesis of Ordered Mesoporous Li−Mn−O Spinel as a Positive Electrode for Rechargeable Lithium Batteries. *Angew. Chem., Int. Ed.* **2008**, *47*, 9711−9716.

(36) Park, B. G.; Ryu, J. H.; Choi, W. Y.; Park, Y. J. Fabrication of 3-Dimensional $LiMn_2O_4$ Thin Film. *Bull. Korean Chem. Soc.* **2009**, *30*, 653−656.

(37) Brezesinski, T.; Wang, J.; Polleux, J.; Dunn, B.; Tolbert, S. H. Templated Nanocrystal-Based Porous TiO_2 Films for Next-Generation Electrochemical Capacitors. *J. Am. Chem. Soc.* **2009**, *131*, 1802−1809.

(38) Rauda, I. E.; Buonsanti, R.; Saldarriaga-Lopez, L. C.; Benjauthrit, K.; Schelhas, L. T.; Stefik, M.; Augustyn, V.; Ko, J.; Dunn, B.; Wiesner, U.; Milliron, D. J.; Tolbert, S. H. A General Method for the Synthesis of Hierarchical Nanocrystal-Based Mesoporous Materials. *ACS Nano* **2012**, *6*, 6386−6399.

(39) Rauda, I. E.; Saldarriaga-Lopez, L. C.; Helms, B. A.; Schelhas, L. T.; Membreno, D.; Milliron, D. J.; Tolbert, S. H. Nanoporous Semiconductors Synthesized Through Polymer Templating of Ligand-Stripped CdSe Nanocrystals. *Adv. Mater.* **2013**, *25*, 1315−1322.

(40) Warren, S. C.; Messina, L. C.; Slaughter, L. S.; Kamperman, M.; Zhou, Q.; Gruner, S. M.; DiSalvo, F. J.; Wiesner, U. Ordered Mesoporous Materials from Metal Nanoparticle−Block Copolymer Self-Assembly. *Science* **2008**, *320*, 1748−1752.

(41) Deshpande, A. S.; Pinna, N.; Smarsly, B.; Antonietti, M.; Niederberger, M. Controlled Assembly of Preformed Ceria Nanocrystals into Highly Ordered 3D Nanostructures. *Small* **2005**, *1*, 313−316.

(42) Ba, J. H.; Polleux, J.; Antonietti, M.; Niederberger, M. Non-Aqueous Synthesis of Tin Oxide Nanocrystals and Their Assembly into Ordered Porous Mesostructures. *Adv. Mater.* **2005**, *17*, 2509−2512.

(43) Dong, A.; Ye, X.; Chen, J.; Kang, Y.; Gordon, T.; Kikkawa, J. M.; Murray, C. B. A Generalized Ligand-Exchange Strategy Enabling Sequential Surface Functionalization of Colloidal Nanocrystals. *J. Am. Chem. Soc.* **2011**, *133*, 998−1006.

(44) Zhang, X.; Xing, Z.; Yu, Y.; Li, Q.; Tang, K.; Huang, T.; Zhu, Y.; Qian, Y.; Chen, D. Synthesis of Mn_3O_4 Nanowires and Their Transformation to $LiMn_2O_4$ Polyhedrons, Application of $LiMn_2O_4$ As a Cathode In a Lithium-Ion Battery. *CrystEngComm* **2012**, *14*, 1485−1489.

(45) Myung, S. TS.; Komaba, S.; Kumagai, N. Hydrothermal Synthesis and Electrochemical Behavior of Orthorhombic $LiMnO_2$. *Electrochim. Acta* **2002**, *47*, 3287−3295.

(46) Li, P.; Nan, C. Y.; Wei, Z.; Lu, J.; Peng, Q.; Li, Y. D. Mn_3O_4 Nanocrystals: Facile Synthesis, Controlled Assembly, and Application. *Chem. Mater.* **2010**, *22*, 4232−4236.

(47) Ju, S. H.; Kim, D. Y.; JO, E. B.; Kang, Y. C. $LiMn_2O_4$ Powders Prepared from Nano-Sized Manganese Oxide Powders. *J. Ceram. Soc. Jpn.* **2007**, *115*, 241−244.

(48) Sun, S.; Murray, C. B. Synthesis of Monodisperse Cobalt Nanocrystals and Their Assembly into Magnetic Superlattices. *J. Appl. Phys.* **1999**, *85*, 4325−4330.

(49) Boyer, J.-C.; Vetrone, F.; Cuccia, L. A.; Capobianco, J. A. Synthesis of Colloidal Upconverting $NaYF_4$ Nanocrystals Doped with Er^{3+}, Yb^{3+} and Tm^{3+}, Yb^{3+} *via* Thermal Decomposition of Lanthanide Trifluoroacetate Precursors. *J. Am. Chem. Soc.* **2006**, *128*, 7444−7445.

(50) Shevchenko, E. V.; Talapin, D. V.; Rogach, A. L.; Kornowski, A.; Haase, M.; Weller, H. Colloidal Synthesis and Self-Assembly of $CoPt_3$ Nanocrystals. *J. Am. Chem. Soc.* **2002**, *124*, 11480−11485.

(51) Manna, L.; Milliron, D. J.; Meisel, A.; Scher, E. C.; Alivisatos, A. P. Controlled Growth of Tetrapod-Branched Inorganic Nanocrystals. *Nat. Mater.* **2003**, *2*, 382−385.

(52) Hines, M. A.; Guyot-Sionnest, P. Synthesis and Characterization of Strongly Luminescing ZnS-Capped CdSe Nanocrystals. *J. Phys. Chem.* **1996**, *100*, 468−471.
(53) Peng, X.; Schlamp, M. C.; Kadavanich, A. V.; Alivisatos, A. P. Epitaxial Growth of Highly Luminescent CdSe/CdS Core/Shell Nanocrystals with Photostability and Electronic Accessibility. *J. Am. Chem. Soc.* **1997**, *119*, 7019−7029.
(54) Xia, Y.; Xiong, Y. J.; Lim, B.; Skrabalak, S. E. Shape-Controlled Synthesis of Metal Nanocrystals: Simple Chemistry Meets Complex Physics? *Angew. Chem., Int. Ed.* **2009**, *48*, 60−103.
(55) Yu, W. W.; Falkner, J. C.; Shih, B. S.; Colvin, V. L. Preparation and Characterization of Monodisperse PbSe Semiconductor Nanocrystals in a Noncoordinating Solvent. *Chem. Mater.* **2004**, *16*, 3318−3322.
(56) Murray, C. B.; Norris, D. J.; Bawendi, M. G. Synthesis and Characterization of Nearly Monodisperse CdE (E = Sulfur, Selenium, Tellurium) Semiconductor Nanocrystallites. *J. Am. Chem. Soc.* **1993**, *115*, 8706−8715.
(57) Chen, O.; Chen, X.; Yang, Y.; Lynch, J.; Wu, H.; Zhuang, J.; Cao, Y. C. Synthesis of Metal-Selenide Nanocrystals Using Selenium Dioxide As the Selenium Precursor. *Angew. Chem., Int. Ed.* **2008**, *47*, 8638−8641.
(58) Sun, Y.; Xia, Y. Shape-Controlled Synthesis of Gold and Silver Nanoparticles. *Science* **2002**, *298*, 2176−2179.
(59) Peng, X.; Manna, L.; Yang, W.; Wickham, J.; Scher, E.; Kadavanich, A.; Alivisatos, A. P. Shape Control of CdSe Nanocrystals. *Nature* **2000**, *404*, 59−61.
(60) Gaponik, N.; Talapin, D. V.; Rogach, A. L.; Hoppe, K.; Shevchenko, E. V.; Kornowski, A.; Eychmuller, A.; Weller, H. Thiol-Capping of CdTe Nanocrystals: An Alternative to Organometallic Synthetic Routes. *J. Phys. Chem. B* **2002**, *106*, 7177−7185.
(61) Talapin, D. V.; Yu, H.; Shevchenko, E. V.; Lobo, A.; Murray, C. B. Synthesis of Colloidal PbSe/PbS Core-Shell Nanowires and PbS/Au Nanowire_Nanocrystal Heterostructures. *J. Phys. Chem. C* **2007**, *111*, 14049−14054.
(62) Yu, T.; Moon, J.; Park, J.; Park, Y. I.; Na, H. B.; Kim, B. H.; Song, I. C.; Moon, W. K.; Hyeon, T. Various-Shaped Uniform Mn_3O_4 Nanocrystals Synthesized at Low Temperature in Air Atmosphere. *Chem. Mater.* **2009**, *21*, 2272−2279.
(63) He, T.; Chen, D.; Jiao, X.; Wang, Y.; Duan, Y. Solubility-Controlled Synthesis of High-Quality Co_3O_4 Nanocrystals. *Chem. Mater.* **2005**, *17*, 4023−4030.
(64) Caruntu, D.; Caruntu, G.; Chen, Y.; O'Connor, C. J.; Goloverda, G.; Kolesnichenko, V. L. Synthesis of Variable-Sized Nanocrystals of Fe_3O_4 with High Surface Reactivity. *Chem. Mater.* **2004**, *16*, 5527−5534.
(65) Thackeray, M. M.; Shao-Horn, Y.; Kahaian, A. J.; Kepler, K. D.; Skinner, E.; Vaughey, J. T.; Hackney, S. A. Structural Fatigue in Spinel Electrodes in High Voltage (4 V) $Li/Li_xMn_2O_4$ Cells. *Electrochem. Solid-State Lett.* **1999**, *1*, 7−9.
(66) Xia, Y.; Yoshio, M. An Investigation of Lithium Ion Insertion into Spinel Structure LiMnO Compounds. *J. Electrochem. Soc.* **1996**, *143*, 825−833.
(67) Huang, H.; Vincent, C. A.; Bruce, P. G. Correlating Capacity Loss of Stoichiometric and Nonstoichiometric Lithium Manganese Oxide Spinel Electrodes with Their Structural Integrity. *J. Electrochem. Soc.* **1999**, *146*, 3649−3654.
(68) Shin, Y.; Manthiram, A. Microstrain and Capacity Fade in Spinel Manganese Oxides. *Electrochem. Solid-State Lett.* **2002**, *5*, A55−A58.
(69) Wills, A. S.; Raju, N. P.; Morin, C.; Greedan, J. E. Two-Dimensional Short-Range Magnetic Order in the Tetragonal Spinel $Li_2Mn_2O_4$. *Chem. Mater.* **1999**, *11*, 1936−1941.
(70) Lee, Y. J.; Wang, F.; Mukerjee, S.; McBreen, J.; Grey, C. P. ^6Li and ^7Li Magic-Angle Spinning Nuclear Magnetic Resonance and *In Situ* X-Ray Diffraction Studies of the Charging and Discharging of $Li_xMn_2O_4$ at 4V. *J. Electrochem. Soc.* **2000**, *147*, 803−812.
(71) Ernst, F. O.; Kammler, H. K.; Roessler, A.; Pratsinis, S. E.; Stark, W. J.; Ufheil, J.; Novák, P. Electrochemically Active Flame-made Nanosized Spinels: $LiMn_2O_4$, $Li_4Ti_5O_{12}$ and $LiFe_5O_8$. *Mater. Chem. Phys.* **2007**, *101*, 372−378.
(72) Patey, T. J.; Büchel, R.; Nakayama, M.; Novák, P. Electrochemistry of $LiMn_2O_4$ Nanoparticles Made by Flame Spray Pyrolysis. *Phys. Chem. Chem. Phys.* **2009**, *11*, 3756−3761.
(73) Rougier, A.; Striebel, K. A.; Wen, S. J.; Cairns, E. I. Cyclic Voltammetry of Pulsed Laser Deposited $Li_xMn_20_4$ Thin Films. *J. Electrochem. Soc.* **1998**, *145*, 2975−2980.
(74) Tang, W.; Tian, S.; Liu, L. L.; Li, L.; Zhang, H. P.; Yue, Y. B.; Bai, Y.; Wu, Y. P.; Zhu, K. Nanochain $LiMn_2O_4$ As Ultra-Fast Cathode Material for Aqueous Rechargeable Lithium Batteries. *Electrochem. Commun.* **2011**, *13*, 205−208.
(75) Jamnik, J.; Maier, J. Nanocrystallinity Effects in Lithium Battery Materials Aspects of Nano-Ionics. Part IV. *Phys. Chem. Chem. Phys.* **2003**, *5*, 5215−5220.
(76) Amos, C. D.; Roldan, M. A.; Varela, M.; Goodenough, J. B.; Ferreira, P. J. Revealing the Reconstructed Surface of $Li[Mn_2]O_4$. *Nano Lett.* **2016**, *16*, 2899−2906.
(77) Karim, A.; Fosse, S.; Persson, K. A. Surface Structure and Equilibrium Particle Shape of the $LiMn_2O_4$ Spinel from First-Principles Calculations. *Phys. Rev. B: Condens. Matter Mater. Phys.* **2013**, *87*, 075322.
(78) Benedek, R.; Thackeray, M. M. Simulation of the Surface Structure of Lithium Manganese Oxide Spinel. *Phys. Rev. B: Condens. Matter Mater. Phys.* **2011**, *83*, 195439.
(79) Pandolfo, A. G.; Hollenkamp, A. F. Carbon Properties and Their Role in Supercapacitors. *J. Power Sources* **2006**, *157*, 11−27.
(80) Conway, B. E. *Electrochemical Supercapacitors: Scientific Fundamentals and Technological Applications*; Springer: Berlin, 1999; p 736.
(81) Angerstein-Kozlowska, H.; Klinger, J.; Conway, B. E. Computer Simulation of the Kinetic Behaviour of Surface Reactions Driven by a Linear Potential Sweep: Part I. Model 1-Electron Reaction with a Single Adsorbed Species. *J. Electroanal. Chem. Interfacial Electrochem.* **1977**, *75*, 45−60.
(82) Lindström, H.; Södergren, S.; Solbrand, A.; Rensmo, H.; Hjelm, J.; Hagfeldt, A.; Lindquist, S. E. Li^+ Ion Insertion in TiO_2 (Anatase). 2. Voltammetry on Nanoporous Films. *J. Phys. Chem. B* **1997**, *101*, 7717−7722.
(83) Tang, X.-C.; Song, X.-W.; Shen, P.-Z.; Jia, D.-Z. Capacity Intermittent Titration Technique (CITT): A Novel Technique for Determination of Li^+ Solid Diffusion Coefficient of $LiMn_2O_4$. *Electrochim. Acta* **2005**, *50*, 5581−5587.
(84) Eftekhari, A. Electrochemical Behavior of Thin-Film $LiMn_2O_4$ Electrode in Aqueous Media. *Electrochim. Acta* **2001**, *47*, 495−499.
(85) Lee, M. H.; Kang, Y. J.; Myung, S. T.; Sun, Y. K. Synthetic Optimization of $Li[Ni_{1/3}Co_{1/3}Mn_{1/3}]O_2$ *via* Co-Precipitation. *Electrochim. Acta* **2004**, *50*, 939−948.
(86) Kim, J. H.; Myung, S. T.; Yoon, C. S.; Kang, S. G.; Sun, Y. K. Comparative Study of $LiNi_{0.5}Mn_{1.5}O_{4-\delta}$ and $LiNi_{0.5}Mn_{1.5}O_4$ Cathodes Having Two Crystallographic Structures: $Fd\bar{3}m$ and $P4_332$. *Chem. Mater.* **2004**, *16*, 906−914.